Research Square

Preprints are preliminary reports that have not undergone peer review.
They should not be considered conclusive, used to inform clinical practice,
or referenced by the media as validated information.

Lattice-oxygen topology engineering to enable durable and high-efficiency aqueous manganese batteries

Hong Jin Fan

fanhj@ntu.edu.sg

Nanyang Technological University https://orcid.org/0000-0003-1237-4555

Zefang Yang

Fudan University

Yuhang Liu

Fudan University

Jinchi Li

Fudan University

Lin Liu

Fudan University

Yifeng Wang

Fudan University https://orcid.org/0009-0004-9148-7615

Fulong Zhu

Fudan University

Hongrun Jin

Laboratory of Advanced Materials, Aqueous Battery Center, Shanghai Key Laboratory of Molecular Catalysis and Innovative Materials, Faculty of Chemistry and Materials, Fudan University, Shanghai 2004

Wanhai Zhou

Fudan University https://orcid.org/0000-0003-3197-9971

Yonggang Wang

Fudan University https://orcid.org/0000-0002-2447-4679

Dongyuan Zhao

Fudan University; Inner Mongolia University https://orcid.org/0000-0001-8440-6902

Dongliang Chao

Fudan University https://orcid.org/0000-0001-7793-0044

Article

Keywords: Aqueous batteries; Electrolytic batteries; Mn2+/MnO2 chemistry; Disproportionation; Lattice oxygen topology

Posted Date: October 28th, 2026

DOI: https://doi.org/10.21203/rs.3.rs-9577726/v1

License: This work is licensed under a Creative Commons Attribution 4.0 International License.
Read Full License

Additional Declarations: There is **NO** Competing Interest.

Lattice-oxygen topology engineering to enable durable and high-efficiency aqueous manganese batteries

Zefang Yang,[1 2] Yuhang Liu,[1] Jinchi Li,[1] Lin Liu,[1] Yifeng Wang,[1] Fulong Zhu,[1] Hongrun Jin,[1] Wanhai Zhou,[1] Yonggang Wang,[3] Hong Jin Fan,*[2] Dongyuan Zhao,[1] Dongliang Chao*[1]

[1]Laboratory of Advanced Materials, Aqueous Battery Center, State Key Laboratory of Molecular Engineering of Polymers, College of Smart Materials and Future Energy, Fudan University, Shanghai, 200433, P. R. China

E-mail: chaod@fudan.edu.cn

[2]School of Physical and Mathematical Sciences, Nanyang Technological University, Singapore 637371, Singapore

E-mail: fanhj@ntu.edu.sg

[3]Department of Chemistry and Shanghai Key Laboratory of Molecular Catalysis and Innovative Materials, Institute of New Energy, iChEM (Collaborative Innovation Center of Chemistry for Energy Materials), Fudan University, Shanghai 200433, P. R. China

Keywords: Aqueous batteries; Electrolytic batteries; Mn^{2+}/MnO_2 chemistry; Disproportionation; Lattice oxygen topology

Abstract

Aqueous manganese batteries based on MnO_2 electrodeposition-dissolution process offer a compelling route to safe, low-cost and scalable energy storage. Despite their merits of high specific capacity and voltage, the hindrance towards practical implementation is the parasitic reaction and accumulation of dead manganese, leading to poor reversibility and low energy efficiency. Here, we identify the lattice-oxygen topology as the structural origin of Mn^{3+}-driven parasitic reaction during weakly acidic MnO_2 dissolution. By synthesizing a series of MnO_2 polymorphs with a controllable transition from pyramidal (O_{py}) to planar oxygen (O_{pl}) topology, we reveal that the rapid O_{py} dissolution accounts for the formation of MnOOH intermediates (i.e., Mn^{3+}), but MnOOH is suppressed on O_{pl}-dominated pathways owing to the larger lattice distortion. Guided by this mechanism, a facile and cost-effective approach is applied to realize dual-regulation of oxygen topology, namely, activating O_{pl} dissolution and simultaneously passivating O_{py} sites through strengthened Mn-O bonding. As a result of the suppressed Mn^{3+} disproportionation side reaction, the Mn-Cu cell retains 100% capacity over 5800 cycles with an energy efficiency of 83% and Coulombic efficiency close to 99.99%. This study unlocks the potential of aqueous manganese oxide batteries for highly durable and sustainable energy storage.

Introduction

Integrating variable renewable energy into power systems requires energy storage units that are fire-free, cost-effective in manufacturing, and environmentally friendly[1–3]. Among emerging aqueous batteries, manganese batteries working on the basis of manganese dioxide (MnO_2) electrodeposition-dissolution have re-emerged as a compelling charge storage system, owing to its high specific capacity (616 mAh g^{-1}), high output voltage (1.23 V vs standard hydrogen electrode), relatively simple electrode architecture compared to conventional rocking-chair batteries, and low-cost, non-toxic and earth-abundant materials[4,5]. Despite rapid advances in recent years, key issues in insufficient cycle life and energy efficiency (EE) should be resolved before this type of battery can be implemented by industry. The stability of electrochemical MnO_2 remains fundamentally constrained by poor electronic conductivity, sluggish reaction kinetics, and persistent accumulation of electrochemically inert dead manganese, resulting in sequestration of active manganese and accelerated polarization[6–8]. Transient Mn^{3+} species typically are generated during MnO_2 reduction, which are subject to disproportionation and hydrolysis, yielding inert precipitates that disrupt Mn^{2+}/MnO_2 cycle reversibility[9,10]. Consequently, the battery generally exhibits poor rate performance and diminishing Coulombic efficiency (CE), even when the deposition/dissolution macroscopically appears uniform[11,12]. These phenomena indicate that the primary challenge in electrolytic MnO_2 lies not solely in mass transfer and electrolyte composition, but in the intrinsic structural-kinetic coupling of the MnO_2 itself.

To mitigate these limitations, extensive engineering approaches have been pursued, such as regulating polymorphs to optimize conductivity, designing Mn bonding environments to boost kinetics, and introducing mediators to activate dead manganese[13–18]. While these methods can improve apparent kinetics and cycling stability, the root causes to the limitations and the mitigation mechanisms have been largely unclear. *Why does MnO_2 exhibit inherently slow and non-uniform dissolution, and why does the Mn^{3+} disproportionation reaction preferentially occur, generating dead manganese during dissolution*? Answering these questions requires a structural descriptor linking MnO_2 polymorphs to reaction pathways. In the MnO_2 polymorphs, a unifying hallmark is the network of edge- and corner-shared Mn-O_6 octahedra. As illustrated in **Fig. 1a**, this framework naturally defines two topologically distinct lattice oxygen environments: pyramidal oxygen (O_{py}) and planar oxygen (O_{pl})[19,20]. This corresponds to two different dissolution mechanisms involving distinct lattice oxygen (**Fig. 1b**). In this context, local bond breaking of lattice oxygen may play a crucial role in intermediate formation and Mn^{3+} parasitic pathways during MnO_2 dissolution[21,22]. However, lattice oxygen topology has rarely been considered as a quantitative variable in aqueous manganese chemistry, and the kinetic competition between these dissolution paths remains unknown.

Here, we aim to unravel the core reason and provide a mitigation solution to the poor MnO_2/Mn^{2+} reversibility in aqueous electrolytic batteries. First, lattice oxygen topology is identified as the structural root of Mn^{3+} disproportionation reactions in weakly acidic MnO_2 dissolution chemistry. By

constructing a controlled material transition from γ-MnO_2 to β-MnO_2, we quantitatively evaluate O_{py} and O_{pl} as independent descriptors. It is found that the dissolution kinetics of O_{py} are faster than those of O_{pl}, preferentially driving the formation of MnOOH intermediates that promote Mn^{3+} disproportionation to produce dead manganese. In contrast, the O_{pl}-dominated dissolution process undergoes a transient Mn*OOH adsorbed state without triggering Mn^{3+} disproportionation reactions. This new insight guides us to engineer the MnO_2 to mitigate the kinetic and reversibility issues, motivating the design of an oxygen-topology strategy to promote the Mn^{2+}/MnO_2 reversibility and reduce dead manganese. As a case study, we engineer MnO_2 cathodes using a non-ionic surfactant, allowing a galvanostatic charge protocol instead of the conventional constant voltage protocol. As a result, the fabricated Mn-Cu battery shows much more stable capacity during longer cycles together with higher EE than the non-engineered MnO_2 cathode. This research may advance the progress of low-cost and high-efficiency aqueous manganese batteries for practical sustainable energy storage.

Results and discussion

Characterization of MnO_2 polymorphs

MnO_2 has a variety of morphologies, including α-, β-, γ-, δ-, λ-, and ε-MnO_2, all of which are composed of Mn-O_6 octahedra interconnected through edge- and corner-sharing (Supplementary Fig. 1)[23]. γ-, δ-, and ε-type MnO_2 can be obtained through electrodeposition in an electrolytic MnO_2 cell. Taking ε-MnO_2 commonly formed in sulfate solutions as an example, the ideal structure consists exclusively of edge-sharing Mn-O_6 octahedra without tunnel features[17]. However, the real electrolytic ε-MnO_2 adopts a NiAs-type structure with a Mn^{4+} cation randomly occupying 50% of the O octahedral centers (Supplementary Fig. 2)[24,25]. This structure disorder results in a random distribution of tunnel- and layer-like motifs in ε-MnO_2 with both edge-sharing (Mn-Mn_{edge}) and corner-sharing (Mn-Mn_{corner}) Mn-O_6 octahedra (Supplementary Fig. 3). To elucidate the role of lattice oxygen in ε-MnO_2 dissolution, we prepared a series of MnO_2 samples with systematically varied lattice oxygen concentrations from γ-type (50% of Mn-Mn_{corner}) to β-type (100% of Mn-Mn_{corner}) via electrodeposition followed by annealing.

First, MnO_2 was prepared via galvanostatic electrodeposition in a water bath at 90 °C (denoted as A90), and followed by annealing at 150, 300, and 400 °C to obtain A150, A300, and A400, respectively. X-ray diffraction (XRD) analysis shows A90 is indexed as γ-MnO_2 (Supplementary Fig. 4). With increasing annealing temperature, two pairs of double peaks in γ-MnO_2 are gradually merged into two single peaks, indicating a transition from ramsdellite to pyrolusite (**Fig. 1c**). To quantify the Mn-Mn_{edge} and Mn-Mn_{corner} ratio in the prepared MnO_2 polymorphs, benchtop-based X-ray absorption fine structure (XAFS) spectroscopy was performed with structural modeling and fitting (Supplementary Fig. 5). Fourier-transform extended XAFS (EXAFS) spectroscopy shows two peaks approximately at 2.51 and 3.13 Å, corresponding to Mn-Mn_{edge} and Mn-Mn_{corner} pairs, respectively (**Fig. 1d**). The calculated Mn-Mn_{corner} fraction rises from 46% to 69% upon increasing the annealing

temperature from 0 to 400 °C (**Fig. 1e** and Supplementary Fig. 6, and Supplementary Table 1). The O_{pl} concentration in A90 is estimated to be 45% via linear interpolation (Supplementary Fig. 7) and increases to 82% at an annealing temperature of 400 °C. X-ray photoelectron spectroscopy (XPS) reveals an increase in O_{pl} concentration with rising annealing temperature, indicating a parallel trend in O_{pl} content across both surface and bulk phases of these MnO_2 polymorphs (Supplementary Fig. 8 and Supplementary Table 2). The deviation in O_{pl} concentration determined by EXAFS and XPS is estimated to be less than 8% (**Fig. 1e**). The Mn oxidation state increases from 3.6 to 3.83 with rising annealing temperature based on X-ray absorption near-edge structure (XANES) spectroscopy (Supplementary Fig. 9). The Mn 2p XPS spectrum also shows an enhancement in Mn^{4+} ion content from 76.1% to 82.5% (Supplementary Fig. 10 and Supplementary Table 3)[26]. γ-MnO_2 presents a flower-like structure composed of nanoneedles and nanoparticles in the scanning electron microscope (SEM) images (Supplementary Fig. 11), with no significant morphological changes after annealing. This characterization proves the successful synthesis of MnO_2 samples with progressively increased O_{pl} concentrations. We also tried to prepare MnO_2 with higher O_{pl} concentrations by increasing the annealing temperature but failed because MnO_2 tends to transform to Mn_3O_4 at high temperatures, which has been demonstrated to be a poorly stable product under acidic conditions (Supplementary Fig. 12)[27].

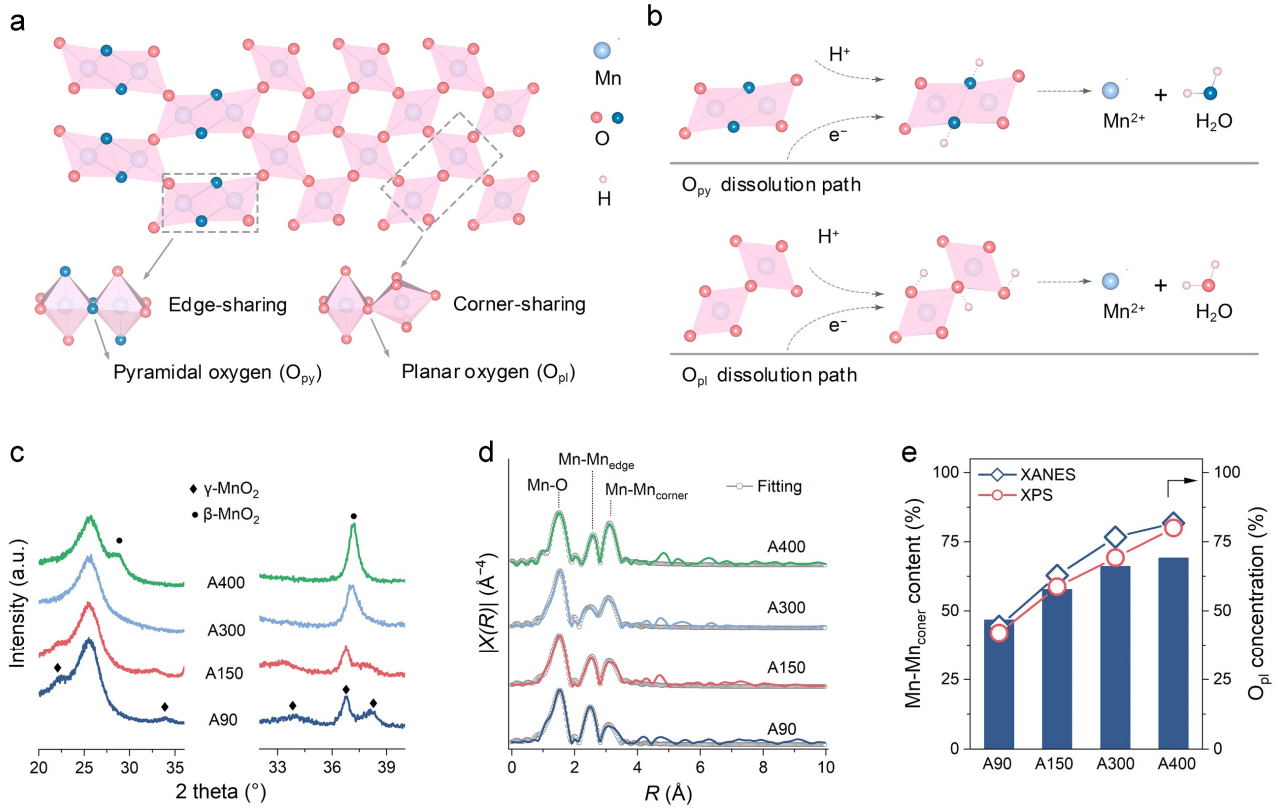


Fig. 1 Dissolution path and characterization of MnO_2 polymorphs. (a) Schematic of MnO_2 atomic structure showing two types of oxygen coordination: pyramidal oxygen (O_{py}) and planar oxygen (O_{pl}).

(b) The corresponding two dissolution paths. (c) XRD patterns of A90, A150, A300 and A400 samples with the reference of γ-MnO_2 and β-MnO_2. (d) Fourier-transformed Mn K-edge EXAFS of A90, A150, A300 and A400 samples. (e) O_{pl} concentration derived from Mn K-edge EXAFS and O 1s XPS of A90, A150, A300 and A400 samples.

Dissolution behavior of MnO_2 polymorphs

To investigate the dissolution behavior of MnO_2 polymorphs, electrochemical measurements were performed in Mn-Cu cells. The discharge profiles show that the extended voltage plateau in A90 gradually declines with the transition from γ-type to β-type structure, accompanied by an increase in reversible capacity (**Fig. 2a**). A short voltage plateau at 0.79 V is observed in A90, corresponding to a new peak generated in the differential capacitance plots, but it gradually disappears at high O_{pl} concentrations. In situ Raman spectroscopy was employed to probe structural evolution during MnO_2 dissolution. A Raman band at 623 cm^{-1} is assigned to Mn-O stretching vibrations in Mn-O_6 octahedra (**Fig. 2b** and Supplementary Fig. 13)[28]. A redshift of 9.9 cm^{-1} is displayed in the in-situ Raman spectrum of A90 during discharge, suggesting a conversion from MnO_2 to MnOOH, as evidenced by the Mn-O stretching vibration of the MnOOH intermediate at 614.8 cm^{-1}. In contrast, the MnOOH formation in A400 is strongly suppressed as reflected by a minimal red shift (1.2 cm^{-1})[29]. Consistently, the MnOOH characteristic peak slowly intensifies in the in-situ XRD pattern of A90 during discharge (Supplementary Fig. 14). XPS spectra further reveal the formation of dead manganese in A90 after deep discharge due to disproportionation reactions of Mn^{3+} ions resulting from MnOOH chemical dissolution (Supplementary Fig. 15)[30]. In refined Mn 2p XPS spectra, the Mn^{3+} species content in A90 during discharge is higher than in A400 and further increases after discharge to 0.75 V (Supplementary Fig. 16 and Supplementary Table 4)[31]. Ion fragments of MnO_2 after discharge to 0.75 V were captured via time-of-flight secondary ion mass spectrometry (TOF-SIMS). The OH^- and OOH^- fragment contents in A90 are higher than those in A400, suggesting accelerated MnOOH formation in A90 after discharge to 0.79 V (Supplementary Fig. 17). These results indicate that γ-MnO_2 is more prone to form MnOOH than β-MnO_2 during conversion of MnO_2 to Mn^{2+}, contributing to an extra shoulder platform in the discharge profiles[32].

To discern the dissolution kinetics of lattice oxygen, in situ synchrotron-based XAFS spectroscopy on MnO_2 dissolution was performed. During discharge, the edge energy (energy value at normalized absorption step height of 0.5) of A90 shifts to lower energy by 0.87 eV, smaller than that observed for A400 (1.46 eV), suggesting a higher average manganese oxidation state in A90 arising from the formation of MnOOH intermediates (**Fig. 2c** and Supplementary Fig. 18)[33]. Fourier-transformed EXAFS spectra show gradual attenuation in the peak intensities for Mn-Mn and Mn-O pairs during discharge, indicating progressive degradation of the Mn-O_6 octahedral structure. The reduction in peak intensity is more pronounced for Mn-Mn_{edge} (0.38) than for Mn-Mn_{corner} (0.23),

suggesting two distinct dissolution pathways involving different lattice oxygen species (**Fig. 2d**). The dissolution of O_{py} ($k_1 = -0.85$) is faster than that of O_{pl} ($k_2 = -0.58$), as determined by linear fitting of the integrated Mn-Mn content versus state of discharge (Supplementary Fig. 19). The electrochemical processes associated with lattice oxygen dissolution were further analyzed using in situ electrochemical impedance spectroscopy with the distribution of relaxation time (DRT) analysis (Supplementary Fig. 20)[34]. Two peaks in the relaxation time (τ) range from 4.46×10^{-4} to 5.37×10^{-6} s can be assigned to the contact resistance related to proton adsorption (Supplementary Fig. 21)[35,36]. All samples demonstrate an identical τ (1×10^{-5} s) peak corresponding to proton adsorption on surface oxygen sites of MnO_2. However, proton adsorption on lattice oxygen exhibits distinct behavior. The τ for lattice oxygen adsorption increases with O_{pl} concentration, and its resistance also shows an increasing trend (**Fig. 2e** and Supplementary Fig. 22). These results indicate superior dissolution kinetics for O_{py} compared to O_{pl}, which might benefit from the unique structure of γ-MnO_2 with 1×2 tunnels rather than β-MnO_2 with 1×1 tunnels (Supplementary Fig. 23)[37]. The migration of Mn species originating from Mn-Mn_{edge} regions within the electrode is faster than that from Mn-Mn_{corner} regions during dissolution, as shown by the reduced τ values in A90 (Supplementary Fig. 24). Galvanostatic intermittent titration (GITT) measurements further support the favorable diffusion kinetics of Mn^{2+} ions in O_{py}-dominated A90 (**Fig. 2f** and Supplementary Fig. 25). The concentrations of dissolved Mn^{2+} were quantified via inductively coupled plasma atomic emission spectroscopy (ICP-AES). Mn dissolution at Mn-Mn_{edge} is enhanced due to rapid proton adsorption by O_{py} and favorable dissolution kinetics (Supplementary Fig. 26). The results indicate that O_{py}-dominated MnO_2 with fast O_{py} dissolution kinetics tends to form MnOOH during dissolution, leading to the formation of dead manganese both inside and outside the electrode (**Fig. 2g**). Conversely, no dead manganese is produced during the dissolution of O_{pl}-dominated MnO_2 at slow O_{pl} dissolution kinetics.

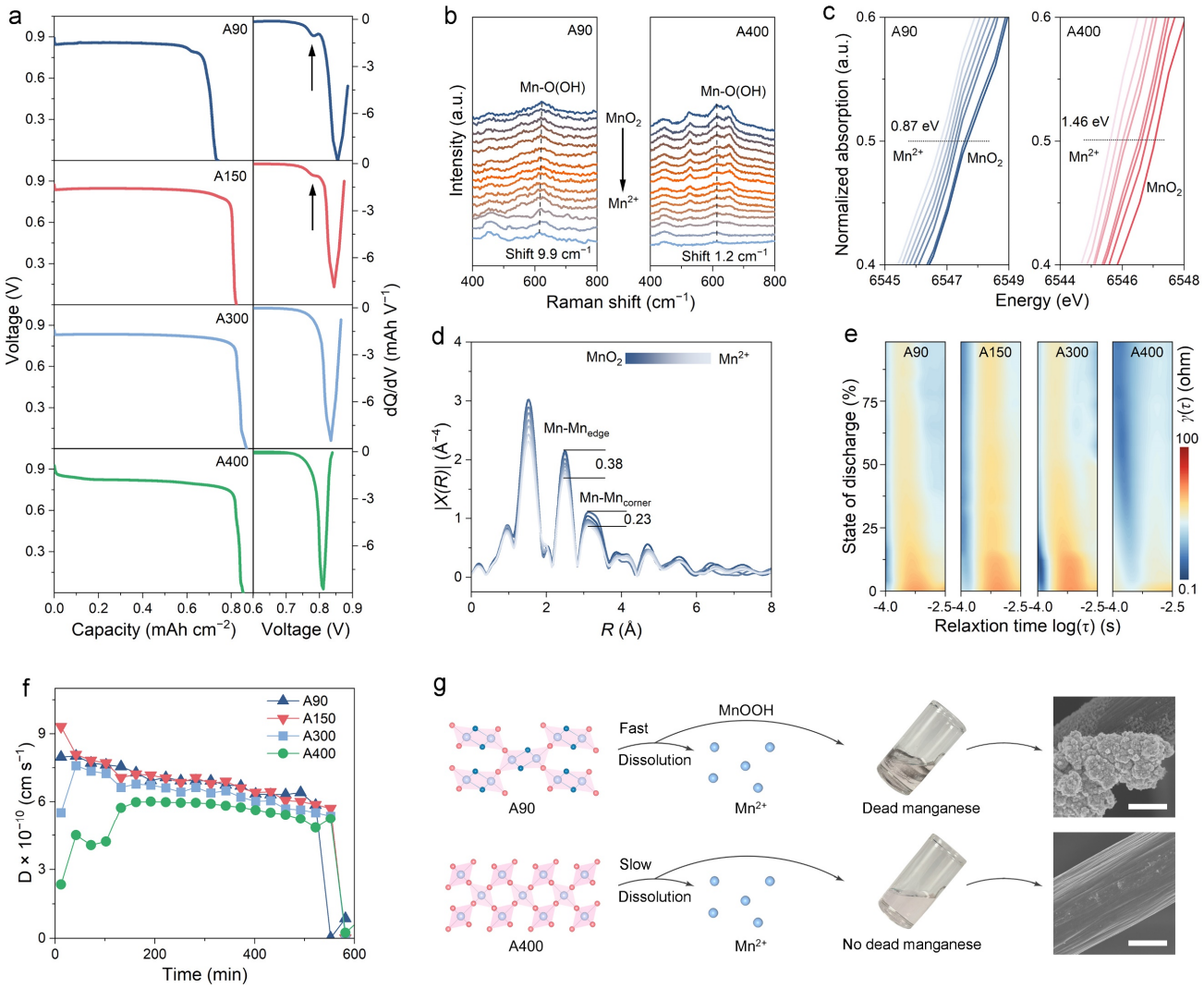


Fig. 2 Dissolution behavior of MnO_2 with different O_{pl} concentrations. (a) The discharge and differential capacitance curves of A90, A150, A300 and A400 samples. (b) In situ Raman spectra and (c) in situ synchrotron Mn K-edge XANES spectra of A90 and A400 samples during dissolution. (d) In situ Fourier-transformed Mn K-edge EXAFS of A90 during dissolution. (e) DRT measurements of A90, A150, A300 and A400 samples during dissolution. (f) The diffusion parameters of Mn^{2+} ions in A90, A150, A300 and A400 samples derived from GITT measurements. (g) Schematic of A90 and A400 dissolution with the evolution of intermediate MnOOH and dead manganese. Shown also are digital graphs of beaker cell after repeated MnO_2 dissolution, and SEM images of the carbon felt after dissolution. Scale bars: 5 μm.

MnO_2 dissolution mechanism involving lattice oxygen

EXAFS analysis (**Fig. 1d** and Supplementary Table 1) reveals a shorter Mn-O_{pl} bond length relative to Mn-O_{py}, indicating that the Mn species may be bound more strongly to O_{pl} than to O_{py}. Density functional theory (DFT) calculations were conducted to analyze the dissolution mechanisms at different lattice oxygen sites. First, the reaction energy barrier for MnO_2 dissolution increases with O_{pl}

concentration (**Fig. 3a** and Supplementary Fig. 27), suggesting that O_{pl} site dissolution is less favorable than O_{py}. A whole dissolution mechanism is proposed wherein MnO_2 separation involves concurrent leaching of surface and lattice oxygen, since only surface oxygen detachment was considered in previous studies (**Fig. 3b** and Supplementary Fig. 28)[18,38–40]. The dissolution rate of MnO_2 is governed by the reaction free energy of the given lattice oxygen dissolution path corresponding to the potential-determining step. Bulk models with O_{pl} concentrations of 50% (A50%), 67% (A67%), 80% (A80%), and 100% (A100%) were constructed to simulate MnO_2 structures with different O_{pl} and O_{py} ratios (Supplementary Fig. 29). **Fig. 3c** presents the free energy diagrams for O_{pl} and O_{py} dissolution mechanisms in MnO_2. The rate-determining step with O_{pl} dissolution is thermodynamically less favorable, exhibiting a reaction free energy approximately 1.35 eV higher than that of O_{py} in A67%, which remains nearly constant even as the O_{pl} concentration increases from 50% to 100% (**Fig. 3d**, Supplementary Figs. 30 and 31). Hence, it can be concluded that the O_{py}-mediated dissolution in MnO_2 with edge- and corner-sharing Mn-O_6 octahedra is favored both thermodynamically and kinetically relative to O_{pl}-mediated dissolution.

The O_{py}-dominated surface exhibits fast proton adsorption kinetics (Supplementary Fig. 24). The desolvation energy of hydrated protons on the O_{py}-dominated surface is also lower than that on the O_{pl}-dominated surface in DFT calculations (Supplementary Fig. 32), which is in favor of the conversion from proton-adsorbed MnO_2 (Mn*OOH) to the MnOOH intermediate (MnOOH(s)). The calculated reaction free energies for MnOOH formation on MnO_2 indicate that MnOOH formation is thermodynamically more favorable on O_{py}-dominated MnO_2 than on O_{pl}-dominated MnO_2 (Supplementary Fig. 33). Besides, MnO_2-to-MnOOH transformation on O_{py}-dominated involves weaker lattice strain of Mn-O_6 octahedra than that on O_{pl}-dominated counterparts (Supplementary Fig. 34). Consequently, a new insight into the dissolution mechanism of MnO_2 governed by lattice oxygen topology is proposed (**Fig. 3e** and Supplementary Note 1). In the O_{py} dissolution mechanism, protons rapidly adsorb onto O_{py} sites of MnO_2 to form Mn*OOH. Subsequently, while Mn*OOH undergoes further proton uptake to form water molecules and dissociate, a competing reaction facilitates the conversion from Mn*OOH to MnOOH. The resulting MnOOH chemically dissolves to Mn^{3+} with proton consumption. The hydrolysis and disproportionation of Mn^{3+} further form inactive MnO_2 inside and outside the electrode, known as dead manganese. However, for the O_{pl} dissolution mechanism, the competing reaction of Mn*OOH to MnOOH is thermodynamically disfavored, which circumvents Mn^{3+} disproportionation and suppresses dead manganese formation. Moreover, the Mn*OOH to MnOOH conversion process for O_{py} is also facilitated by the lower energy 2p state of O_{py} compared to that of O_{pl} (Supplementary Fig. 35). Hence, it can be concluded that guiding dissolution in ε-MnO_2 along the O_{pl} pathway would prevent the occurrence of Mn^{3+} disproportionation and enhance its deposition/dissolution reversibility.

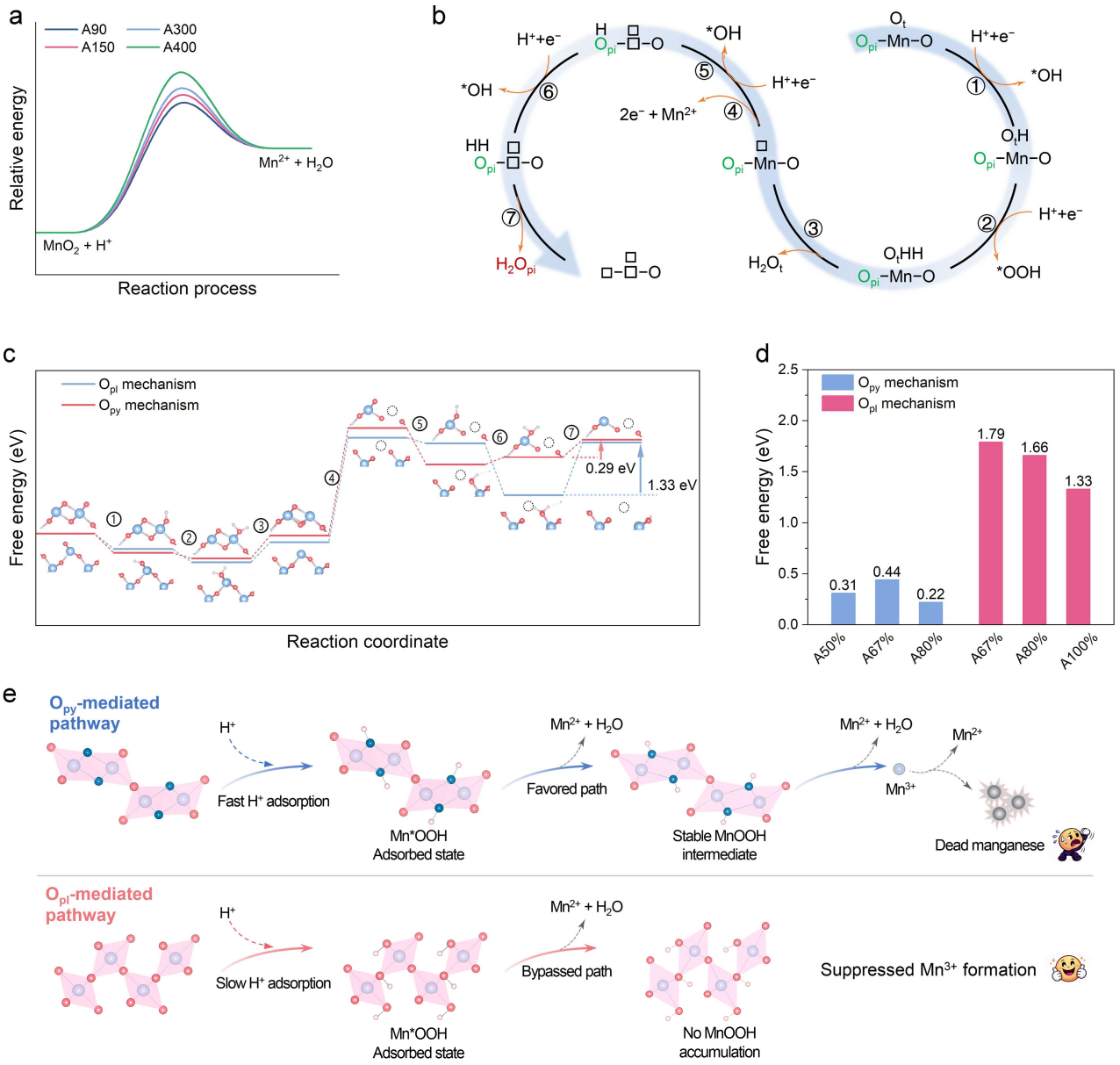


Fig. 3 Lattice oxygen dominated MnO_2 dissolution mechanism. (a) The energy barriers of MnO_2 dissolution with proton into Mn^{2+} and water in the prepared A90, A150, A300 and A400 samples. (b) Schematics of the MnO_2 dissolution mechanism with proton incorporation and separation of manganese and water carrying surface and lattice oxygen. The box symbol refers to the vacancy left when the atoms (Mn, O) are removed from the crystal lattice. (c) Free energy diagrams of MnO_2 dissolution with O_{pl} and O_{py} dissolution path. (d) Calculated free energies of lattice oxygen dissolution in MnO_2 with different O_{pl} concentrations. (e) Schematic illustration of the detailed O_{pl} and O_{py} dissolution mechanisms with and without Mn^{3+} intermediate, respectively.

Electrochemical performances of the Mn-Cu cell

First, the electrochemical performance of Mn-Cu cells using the raw electrolyte (0.7 m $MnSO_4$ and 0.7 m $CuSO_4$ with 0.5 m H_2SO_4) was evaluated at different charging voltages. The CE of Mn-Cu cells

is slightly improved by increasing the potentiostatic charging voltage, which is the commonly used charging protocol in previous reports that can deliver good cycling performance (Supplementary Fig. 36).[5] However, increasing charging voltage has negligible effect on enhancing MnO_2 discharge energy owing to persistent proton consumption induced by Mn^{3+} formation, significantly lowering EE. Consequently, a polyoxyethylene sorbitan monolaurate non-ionic surfactant (TW20) is introduced into the raw electrolyte to implement lattice oxygen-topology regulation. Both EE and CE of MnO_2 deposition/dissolution are improved in a three-electrode cell using TW20 electrolyte (1 m $MnSO_4$ and 0.2 m H_2SO_4 with 0.01 g L^{-1} TW20) under galvanostatic charge and discharge conditions (**Fig. 4a**). The MnOOH intermediate is suppressed upon TW20 incorporation, suggesting its lattice oxygen modulation behavior because the preferential dissolution of O_{pl} is disfavored for the formation of MnOOH (Supplementary Fig. 37). This positive impact is verified using high mass loading of MnO_2 since the electron transport pathways are longer in thick MnO_2 deposition layers (**Fig. 4b** and Supplementary Fig. 38).[17] Even at a charge capacity of 10 mAh cm^{-2}, no MnOOH-related extra discharge plateau is observed in the TW20 electrolyte (**Fig. 4c**). From the cyclic voltammetry (CV) measurements with different scan rates, only a single reduction peak is presented in the TW20 electrolyte (**Fig. 4d**), in contrast to the two reduction peaks in the raw electrolyte. This individual peak is well-maintained during long-term CV profiles, indicating that TW20 induces a steady MnO_2 solid-liquid transition (Supplementary Fig. 39).

To elucidate the practical application of Mn-Cu cells employing TW20, galvanostatic charge-discharge protocol was used to assess the cycling stability. The concentration of TW20 is optimized to 0.01 g L^{-1} (Supplementary Fig. 40). The Mn-Cu cell with TW20 electrolyte exhibits an EE of 83% and an average CE close to 99.99% over 5800 cycles at an areal capacity of 0.5 mAh cm^{-2} (**Fig. 4e** and Supplementary Fig. 41). In contrast, the Mn-Cu batteries using the raw electrolyte gradually lose EE with cycling, retaining about 60% (average CE of 93%) after 1100 cycles. Under a higher capacity (a charge capacity of 2 mAh cm^{-2}), the Mn-Cu cell with TW20 electrolyte shows no obvious degradation in EE (78%) within 400 cycles, compared to the EE of 50% in that using the raw electrolyte (Supplementary Fig. 42). Dual-electrode-free (DEF) cells using carbon felt || Ni foam as the current collectors without active materials on the cathode or anode side are assembled to achieve higher energy density of MnO_2 batteries. The Mn-Cu DEF cells using TW20 electrolyte are cycled at 10 mA cm^{-2} and 1 mAh cm^{-2} for 370 cycles, with an EE of 81% and an average CE of 99.9% (**Fig. 4f** and Supplementary Fig. 43). However, the Mn-Cu DEF cell using the raw electrolyte shows consistently lower efficiency (with EE and CE decreasing to 53% and 91%, respectively, after 370 cycles). When compared to currently prevalent batteries based on Mn^{2+}/MnO_2 conversion, this Mn-Cu battery incorporating TW20 demonstrates evident advantage in terms of cycling stability and EE due to the adoption of a galvanostatic charge protocol instead of constant voltage (**Fig. 4g** and Supplementary Table 5). This outcome is attributed to the homogeneous dissolution of MnO_2 without

intermediate products and the enhanced Cu deposition/dissolution behavior facilitated by TW20 (Supplementary Figs. 44 and 45).

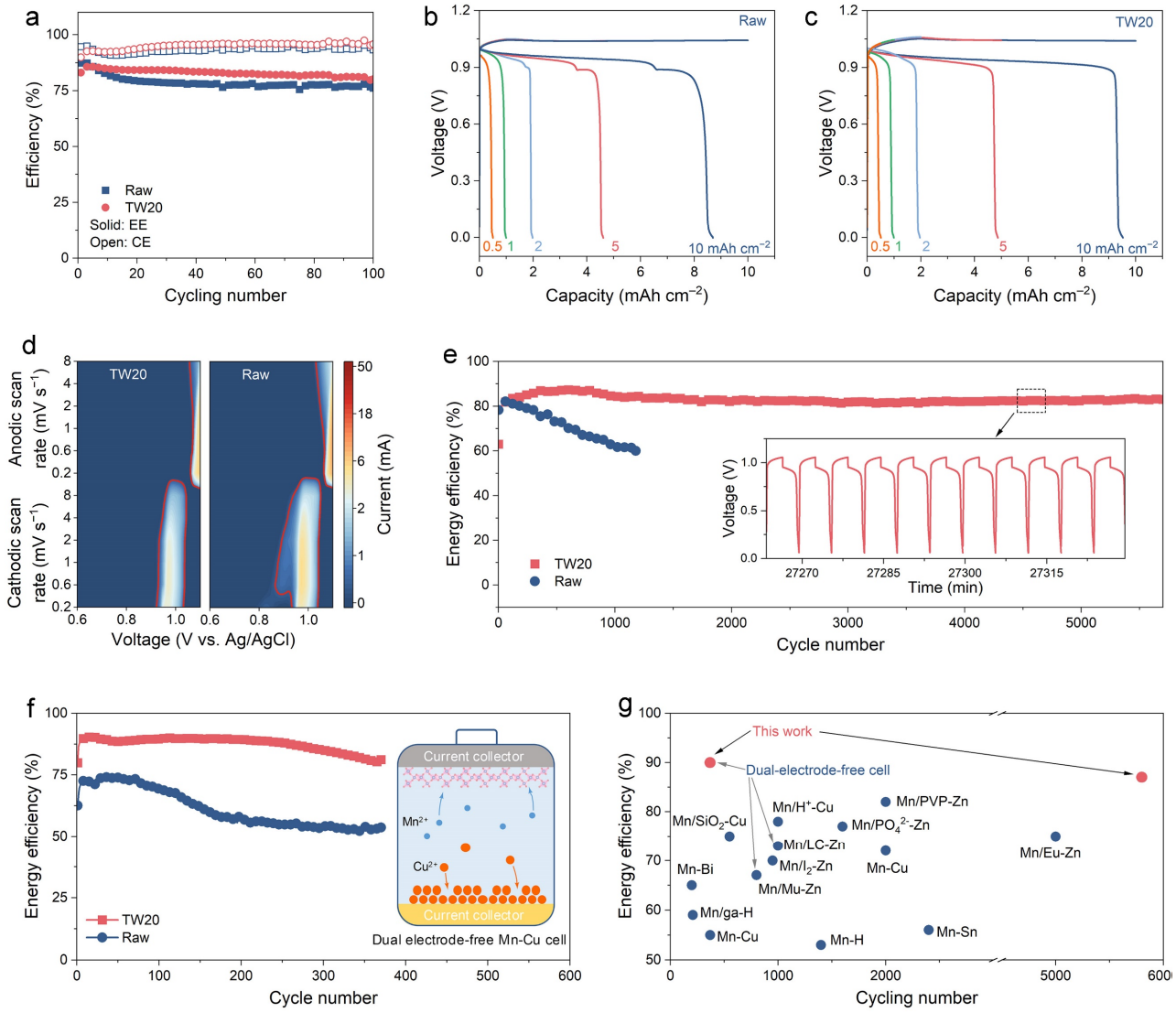


Fig. 4 The electrochemical performance of Mn-Cu cell enhanced by TW20. (a) The CE and EE of MnO_2 deposition/dissolution in a three-electrode cell using raw and TW20 electrolytes at a current density of 1 mA cm^{-2} for 1 mAh cm^{-2}. Voltage curves of Mn-Cu cell using (b) raw and (c) TW20 electrolytes at a current density of 1 mA cm^{-2} for different capacities. (d) CV mapping of MnO_2 deposition/dissolution with TW20 and raw electrolytes at different scan rates. (e) Cycling performance of Mn-Cu cell using TW20 and raw electrolytes at 10 mA cm^{-2} for 0.5 mAh cm^{-2}. (f) Cycling stability of Mn-Cu dual-electrode-free cell using TW20 and raw electrolytes at 10 mA cm^{-2} for 1 mAh cm^{-2}. The inset is a schematic illustration of the Mn-Cu DEF battery. (g) Comparison of EE of this work with previously reported cells based on Mn^{2+}/MnO_2 chemistry.

Verification of electrodissolution promotion mechanism

In situ attenuated total reflection surface-enhanced infrared absorption spectroscopy (ATR-SEIRAS)

was employed to probe the evolution of intermediates during MnO_2 dissolution (Supplementary Fig. 46). As shown in **Fig. 5a** and Supplementary Fig. 47, two distinct bands at 950-1100 and 3000-3700 cm^{-1} in the raw electrolyte were identified as the O-O stretching vibration of *OOH and the O-H vibrational mode of *OH, respectively[41,42]. The intensity of the *OOH peak sharply increases during MnO_2 dissolution in the raw electrolyte. Also, the *OH band exhibits a pronounced shift of 57.3 cm^{-1} from 3414.3 to 3357 cm^{-1} within the raw electrolyte due to strong hydrogen bonding/lattice coupling in the formed MnOOH[43]. However, a negligible increase in *OOH band intensity and a small red shift (27.5 cm^{-1}) of *OH from 3458.5 to 3431 cm^{-1} are observed during MnO_2 discharge in TW20 electrolyte, indicating effective suppression of MnOOH intermediate formation by TW20 (**Fig. 5b**). Chemically dissolved Mn^{3+} species from the formed MnOOH were further detected via in situ UV-vis absorption spectroscopy (Supplementary Fig. 48). The Mn^{3+} content in the electrolysis cell with TW20 shows only minor changes during MnO_2 dissolution, while the cell using raw electrolyte reveals a sharp increase in Mn^{3+} concentration (Supplementary Figs. 49 and 50). Post-cycling XPS, XRD, and SEM analyses further demonstrate that the disproportionation of Mn^{3+} during MnO_2 dissolution is suppressed in the TW20 electrolyte, thus preventing the accumulation of dead manganese (Supplementary Figs. 51-53).

DFT calculations show that TW20 binds more strongly than water to both O_{py} (O_{py} surface) and O_{pl} (O_{pl} surface) dominated ε-MnO_2 surfaces, with binding energies of −0.43 and −0.79 eV on O_{py} and O_{pl} surfaces, respectively, compared with −0.23 and −0.57 eV for water adsorption (**Fig. 5c** and Supplementary Fig. 54). Combined with quartz crystal microbalance (QCM) measurements, the strong interaction between TW20 and ε-MnO_2 is further validated, suggesting preferential adsorption of TW20 versus water molecules on the ε-MnO_2 surface (Supplementary Fig. 55)[44]. The separation energy (E_{sep}) of surface oxygen on the O_{py} surface (1.90 eV) is higher than that on the O_{pl} surface (0.68 eV) upon introduction of TW20 onto the ε-MnO_2 surface (**Fig. 5d**). Furthermore, TW20 incorporation renders O_{py} dissolution in bulk ε-MnO_2 thermodynamically unfavorable, while facilitating O_{pl} separation (Supplementary Fig. 56). The hybridization between Mn 3d and O 2p orbitals at proton-adsorbed O_{py} sites was quantified via analyzing projected density of states (PDOS)[45]. The hybridization degree between Mn 3d and O 2p orbitals at both the surface and lattice oxygen sites increases upon TW20 addition, suggesting enhanced Mn-O bond strength (**Fig. 5e**, Supplementary Fig. 57 and Supplementary Table 6). Based on these results, we propose a TW20-regulated lattice oxygen topological mechanism in ε-MnO_2 dissolution: O_{py} passivation and O_{pl} activation (Supplementary Fig. 58 and Supplementary Note 2). Initially, TW20 molecules strongly interact with ε-MnO_2 and anchor onto both O_{py} and O_{pl} surfaces. Subsequently, surface and lattice oxygen at local O_{pl} surface is activated to facilitate separation during ε-MnO_2 dissolution. Simultaneously, oxygen separation associated with O_{py} at local O_{py} surface is hindered due to strengthened Mn-O bonds, thereby inhibiting MnOOH formation and preventing Mn^{3+} disproportionation reactions since MnOOH formation is

thermodynamically and kinetically favored in O_{py}-dominated MnO_2 during dissolution. The intrinsic O_{py}-preferred dissolution sequence is reprogrammed toward an O_{pl} dissolution pathway through the O_{pl} activation, leading to the transformation of O_{py} sites into non-lattice oxygen (O_{pi}).

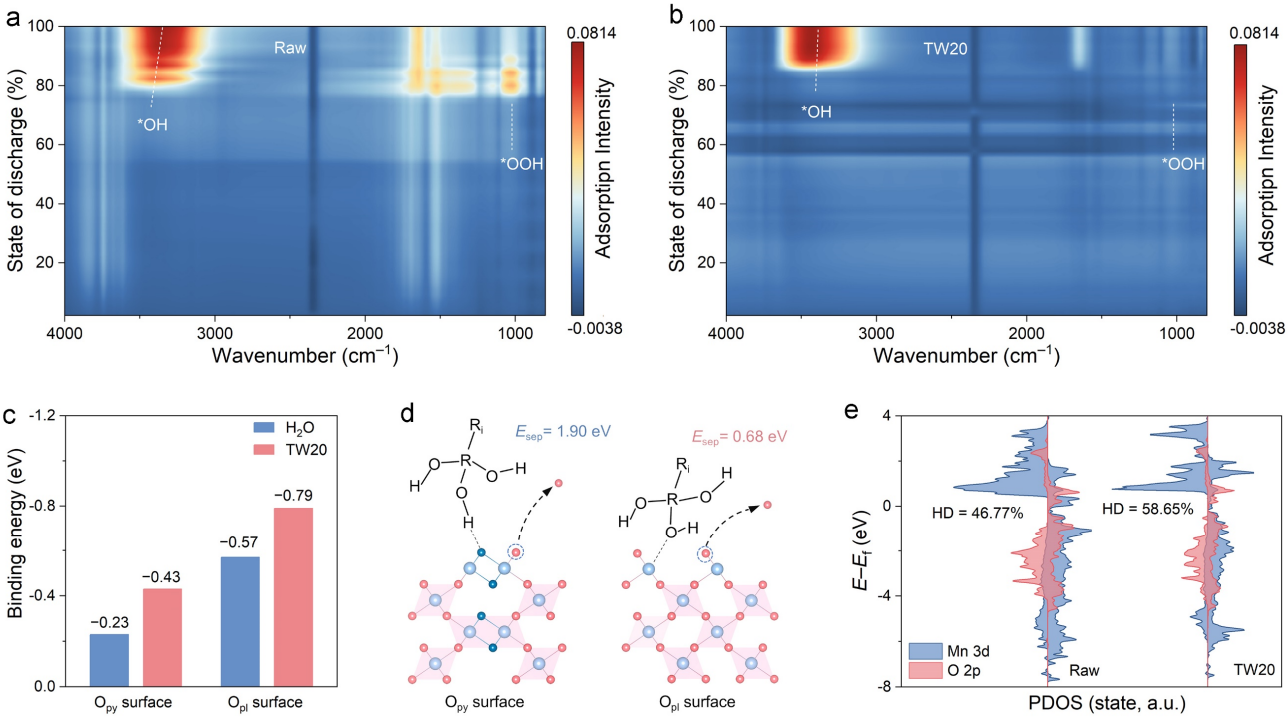


Fig. 5 Verification of promotion mechanism in ε-MnO_2 dissolution due to TW20 regulation. In situ ATR-SEIRAS mapping of MnO_2 dissolution in (a) raw and (b) TW20 electrolytes. (c) Binding energy of TW20 and H_2O molecules on O_{py} and O_{pl} surfaces. (d) Separation energy of surface oxygen from O_{py} surface and O_{pl} with TW20 molecules. After geometry optimization, H atom at OH group in TW20 tends to adsorb on O_{py} sites of O_{py} surface, while Mn sites in O_{pl} surface interact with O atom at OH group in TW20. (e) PDOS diagrams of Mn 3d and O 2p at lattice oxygen in O_{py} surface with and without TW20.

Conclusion

We have established lattice-oxygen topology as a decisive structural descriptor that links MnO_2 structure to dissolution pathways and parasitic Mn^{3+} chemistry during the weakly acidic MnO_2/Mn^{2+} conversion process. A rapid pyramidal oxygen (O_{py})-governed dissolution favors MnOOH formation, which chemically generates Mn^{3+} and accelerates disproportionation, thus accumulating electrochemically inactive dead manganese. Conversely, in the planar oxygen (O_{pl})-dominated dissolution, MnOOH is largely suppressed, leading to diminished parasitic reactions. The distinction between these two dissolution pathways originates from both thermodynamic factor and different lattice strain from MnO_2 to MnOOH. Based on this insight, we implement an oxygen-topology regulation strategy to reprogram the dissolution sequence. Introduction of a non-ionic surfactant is

effective in activating O_{pl} dissolution while passivating O_{py} sites through strengthened Mn-O bonding, thus retaining the MnO_2 deposition/dissolution reversibility for extended cycles. As a result, Mn-Cu cells deliver long-life cycling (>5800 cycles), achieving energy efficiency of 83%, capacity retention and coulombic efficiency of both approximately 99.99%. Prospectively, the facile while effective mitigation solutions showcased in this study may push forward the advancement of aqueous manganese batteries towards next-generation high-safety and sustainable energy storage technology.

Methods

Chemicals and Materials

Manganese sulphate monohydrate ($MnSO_4•H_2O$, AR > 99%), ammonium acetate (CH_3COONH_4, AR), poly(tetrafluoroethylene) (PTFE, 60wt%) and polyoxyethylene (20) sorbitan monolaurate solution (TW20) were procured through Aladdin Biochemical Technology Co., Ltd. Copper sulphate pentahydrate (($CuSO_4•5H_2O$, AR>99%)), anhydrous ethanol (CH_3CH_2OH), potassium permanganate ($KMnO_4$, AR>99.5%) and sulfuric acid (H_2SO_4, 95.0~98.0%) were procured from Sinopharm Chemical Reagent Co., Ltd. Titanium foil and glass fiber separator were procured from Tianjin Annohe New Energy Technology Co., Ltd. Carbon felt was procured from Inner Mongolia Wanxing Carbon Co., Ltd. All reagents were used without purification.

Preparation of MnO_2 polymorph

MnO_2 polymorphs were prepared via conventional electrodeposition methods. First, a 1 m $MnSO_4$ solution mixed with 0.2 m H_2SO_4 was prepared by dissolving $MnSO_4•H_2O$ in deionized water and adding an appropriate amount of H_2SO_4. Electrodeposition on carbon felt was performed in a water bath containing the above mixed solution at 90 °C. The amount of MnO_2 deposition was controlled at a constant current density of 2 mAh cm^{-2} for 0.5 h. The obtained MnO_2 deposit was washed three times with deionized water and ethanol, then dried at 60 °C for 6 h, designated as A90. A90 was further annealed at 150, 300, and 400 °C for 5 h in air, designated as A150, A300, and A400 respectively.

Preparation of MnOOH

$KMnO_4$ and CH_3COONH_4 were dissolved in deionized water via magnetic stirring to obtain a mixed solution of 0.05 m $KMnO_4$ and 0.03 m CH_3COONH_4. 60 mL of the above mixed solution was transferred to a stainless steel autoclave of 100 mL with polytetrafluoroethylene for hydrothermal reaction at 180 °C for 24 h. After cooling to room temperature, the obtained precipitate was washed three times with deionized water and ethanol, then dried at 60 °C for 12 h.

Materials characterizations

The crystal structure of the prepared samples was measured on a Bruker D8 diffractometer with Cu kα radiation (λ = 0.15405 nm) under operating conditions of 40 kV and 40 mA. The Mn oxidation

state was analyzed on a Thermo Scientific ESCALAB QXi X-ray photoelectron spectrometer (4 keV Ar^+). The morphology of MnO_2 was characterized using a Hitachi/SU8600 field emission scanning electron microscope. The lattice oxygen concentration was measured on an hIXAS benchtop-based X-ray absorption fine structure spectrometer from Hp Spectroscopy GmbH. The Mn ion concentration in the electrolyte after MnO_2 dissolution was detected using a PE-8000 inductively coupled plasma (ICP) emission spectrometer. The dissolution of MnOOH intermediate was quantified by the UV-3600 ultraviolet visible (UV-vis) absorption spectrometer (Shimadzu, Japan). Chemical composition and depth distribution information of the post-discharge MnO_2 product were obtained using a PHI nanoTOF 3 time-of-flight secondary ion mass spectrometer (Japan) with a 2 keV Ar^+ ion beam from ULVAC-PHI. In situ Raman spectra during MnO_2 dissolution were collected on an in Via Qontor Raman spectrometer from Renishaw (UK). For in situ Raman spectroscopy testing, MnO_2 prepared on carbon felt was coated onto a conductive substrate within a laboratory-made mold with a Pt wire as the counter electrode and Ag/AgCl as the reference electrode.

QCM measurements

The QCM was performed on an Autolab PGSTAT 128N electrochemical workstation (Metrohm) equipped with a QCM oscillator 70511. Based on the piezoelectric effect of the quartz crystal, the resonance frequency of the Au electrode is sensitive to mass changes. Mass changes can be calculated via the Sauerbrey equation based on the frequency response[46,47].

$$\Delta f = -\frac{2f_0^2}{A\sqrt{\rho_q \mu_q}}\Delta m = -C_f \Delta m \quad (1)$$

where Δf, f_0, Δm, A, C_f, ρ_q and μ_q were the frequency change, crystal fundamental frequency, mass change, area of Au film, mass sensitivity, crystal density and shear modulus, respectively.

ε-MnO_2 deposited on carbon felt was first ground and dispersed in a Nafion aqueous solution. The mixed solution was dropped onto an Au electrode and dried in air. The mass loading of active ε-MnO_2 on the Au electrode ranged from 50 to 100 μg cm^{-2}. QCM testing was performed in a three-electrode system with open-circuit voltage, employing the ε-MnO_2-loaded Au electrode as the working electrode, a Pt wire as the counter electrode, and Ag/AgCl as the reference electrode.

In-situ synchrotron radiation technique

The dissolution of MnO_2 lattice oxygen was investigated via in-situ synchrotron X-ray absorption fine structure spectroscopy (XAFS). In-situ synchrotron XAFS measurements were performed at the BL14B1 beamline of the Shanghai Synchrotron Radiation Facility (SSRF), collected in transmission mode. The cell configuration for in situ measurement consisted of MnO_2 on carbon felt as the working electrode, copper foil as both the counter electrode and reference electrode, a separator and clamping plates. The cell was assembled as a sandwich structure comprising a MnO_2 electrode with a diameter of 14 mm, glass fiber (a diameter of 16 mm) with electrolyte, and a copper foil (a diameter of 14 mm)

with a 10 mm circular aperture. A constant current discharge density of 0.5 mA cm^{-2} was maintained.

In situ attenuated total reflection surface-enhanced infrared absorption spectroscopy (ATR-SEIRAS)

In situ ATR-SEIRAS measurements were performed in a reflection configuration using a FTLA2000-PH40 infrared spectrometer from ABB Canada. A silicon prism was first coated with a thin gold film to serve as the infrared-enhancing substrate. MnO_2 powders were obtained by grinding the as-prepared MnO_2 deposited on carbon felt. 2 mg of MnO_2 and acetylene black powder in a ratio of 9:1 was dispersed in 2 mL of a mixed solution consisting of deionized water and ethanol (volume ratio 1:1), and then 10 μL of Nafion (5wt%) was added in mixed solution with ultrasonication for 2 h to obtain uniform ink. The resulting ink was drop-cast onto the gold-coated silicon prism and dried under ambient conditions. The modified silicon prism was assembled in a custom-made electrochemical cell and employed as the working electrode, with a high-purity platinum wire as the counter electrode and Ag/AgCl as the reference electrode. Electrochemical measurements were conducted in an electrolyte containing 1 m $MnSO_4$ and 0.2 m H_2SO_4 with and without TW20. In situ ATR-SEIRAS spectra were collected during linear sweep voltammetry (LSV) at a scan rate of 0.2 mV s^{-1}, with the potential swept from the open-circuit potential to 0 V (versus Ag/AgCl). The electrolyte was continuously circulated through the cell using a peristaltic pump during testing period.

Electrochemical measurements

The reversible deposition/dissolution of MnO_2 was investigated in a three-electrode beaker cell with carbon felt as the working electrode, activated carbon (AC) as the counter electrode, and Ag/AgCl as the reference electrode. The AC electrode was prepared by mixing AC powder, acetylene black, and poly(tetrafluoroethylene) in a ratio of 8:1:1 to form a plasticine-like mixture in an ethanol-water solvent. The homogeneous mixture was rolled into sheets and dried at 60 °C for 8 h. The Mn-Cu cell was assembled in a custom-made cell using a sandwich structure comprising carbon felt, GF/D glass fiber saturated with electrolyte and Cu foil, on our previous work[18]. The Mn-Cu DEF cell was assembled using the same method as the Mn-Cu cell, except with Ni foam replacing the copper foil. The electrolyte for the three-electrode cell comprised 1 m $MnSO_4$ and 0.2 m H_2SO_4 with and without 0.01 g L^{-1} TW20. For both Mn-Cu and Mn-Ni cells, the electrolyte consisted of 0.7 m $MnSO_4$, 0.7 m $CuSO_4$, and 0.5 m H_2SO_4 with and without 0.01 g L^{-1} TW20. Cu-Cu symmetric cells were assembled using two Cu foils as the cathode and anode, with GF/D glass fiber saturated in 1 m $CuSO_4$ and 0.5 m H_2SO_4, with and without 0.01 g L^{-1} TW20, as the separator. Ni-Cu cells were assembled using the same method as Cu-Cu cells, except with Ni foam replacing the Cu foil cathode.

In situ electrochemical impedance spectroscopy (EIS) was performed for MnO_2 dissolution in Mn-Cu cells under open-circuit voltage conditions at various discharge states. Pulsed discharge was applied at a constant current density of 0.2 mA cm^{-2} for 10 min, followed by 10 min of open-circuit

voltage to stabilize the cell, after which EIS was conducted. This process was repeated until the state of discharge reached 0. The frequency range for EIS testing was set from 100 kHz to 100 mHz at an amplitude of 5 mV. Dissolution of MnO_2 for ICP testing was performed in a three-electrode cell with 0.2 m H_2SO_4 solution at a constant potential of 0.9 V (vs. Ag/AgCl) for 2 h. Charge-discharge cycles with different protocols and galvanostatic intermittent titration technique (GITT) were performed on a Neware battery testing system. GITT was performed using a pulse discharge protocol at 0.2 mA cm^{-2} constant current discharge for 12 min, followed by 18 min of rest to reach equilibrium potential, repeated until the state of discharge reached 0. Tafel curves for the Cu anode were recorded at a scan rate of 1 mV s^{-1} over the voltage range −0.3 to 0.3 V (vs. Cu/Cu^{2+}). Cyclic voltammetry tests for the Mn-Cu cell produced voltage curves from 0 to 1.1 V (vs. Cu/Cu^{2+}) at various scan rates. Tafel and CV measurements were conducted on an EC-lab electrochemical workstation (Biologic VSP-3e, France).

Theoretical calculations

All spin-polarized density functional theory (DFT) calculations were performed using the Vienna ab initio simulation package (VASP)[48]. The exchange-correlation interaction was described within the generalized gradient approximation using the Perdew-Burke-Ernzerhof (GGA-PBE) functional[49]. On-site Coulomb interactions of Mn 3d states were treated using the DFT+U approach with the rotationally invariant formulation (LDAUTYPE = 2), where the effective Hubbard parameter was set to U=3.9 eV for Mn and U=0 eV for O. Long-range dispersion interactions were described using the semi-empirical Grimme D3 correction for van der Waals forces. Structural relaxations were carried out with a plane-wave kinetic energy cutoff of 500 eV until the residual forces on each atom were below 0.01 eV $Å^{-1}$, and the electronic self-consistency convergence criterion was set to 10^{-5} eV. Symmetry was disabled to avoid spurious constraints in slab calculations. A vacuum thickness of 18 Å was employed for free-energy calculations, whereas a larger vacuum region of 35 Å was used for binding and separation energy calculations with TW20 on the MnO_2 surface.

A series of MnO_2 polymorphs with varied O_{py} and O_{pl} oxygen contents were constructed using γ-MnO_2 and β-MnO_2 as structural references. The MnO_2 polymorph dissolution free energy was evaluated by considering the separation process in which protons combine with surface and lattice oxygen to form water[38]. The free-energy change was calculated according to the following equation.

$$\Delta G = \Delta E + \Delta E_{ZPE} - T\Delta S \quad (2)$$

where ΔE is the total-energy difference between the final and initial states, and ΔS is the corresponding changes in zero-point energy and entropy at a temperature 298 K, which are related to vibrational frequency.

To compute the binding energy of TW20 and H_2O on ε-MnO_2 surfaces, O_{py} and O_{pl} dominated surfaces in ε-MnO_2 were constructed by removing Mn atom of the cleaved (001) faceted ε-MnO_2 based

on the random 50% cation vacancy. Binding energy of TW20 and H_2O on O_{py} and O_{pl} surfaces was calculated by the following equation.

$$E_b = E_{total} - E_{slab} - E_{ad} \quad (3)$$

where E_{total}, E_{slab} and E_{ad} were the total energy of adsorbate on surfaces, cleaved surface and adsorbate, respectively. Separation energy of surface oxygen from O_{py} and O_{pl} surfaces with TW20 was calculated by the following equation.

$$E_{sep} = E_{Ov} + E_{H2O} - E_{pr} \quad (4)$$

where E_{pr}, E_{Ov} and E_{H2O} were the total energy of two protons adsorbed at surface oxygen on surfaces with TW20, surface oxygen-removed surfaces with TW20 and a water molecule, respectively.

The variation of Mn-O bond in proton adsorbed on lattice oxygen of ε-MnO_2 with and without TW20 was characterized by calculating the projected density of states (PDOS). The Fermi level was set to 0 eV for DOS alignment.

Notes

The authors declare no competing interest.

Data availability

The authors declare that the data supporting the findings of this work are available within the paper and its Supplementary Information.

Acknowledgements

The authors acknowledge the financial support from the National Key R&D Program of China (2024YFE0101100 and 2022YFA1503501), the National Natural Science Foundation of China (U24A2060, 22088101, 22279023, and 22309031), the Fundamental Research Funds for the Central Universities (20720250005), the Science and Technology Commission of Shanghai Municipality (25DZ3002901, 25DZ3002803, 2024ZDSYS02, 25PY2600100), the Shanghai International Science and Technology Partnership Project (23520750400), the Shanghai Science and Technology Innovation Action Plan Morning Star Project (23YF1401800), the Open Research Fund of the State Key Laboratory of Tropic Ocean Engineering Materials and Materials Evaluation (No. STOEM2025KF021), and the China Postdoctoral Science Foundation (2024M760502). The authors thank the AI for Science Foundation of Fudan University (FudanX24A1035), Shanghai Pilot Program for Basic Research-Fudan University 21TQ1400100 (25TQ012), and the National Research Foundation, Singapore, under its Singapore-China Joint Flagship Project (Clean Energy). The author acknowledges Beijing TOP-UNISTAR Science & Technology Co., Ltd. for their support in XANES and EXAFS measurements. The author also thanks the facility's support of the BL02U2 and BL14W1

beamline of the Shanghai Synchrotron Radiation Facility (SSRF).

References

1. Wang, Q. *et al.* Ionic potential for battery materials. *Nat. Rev. Mater.* **10**, 697–712 (2025).
2. Hu, X. *et al.* External-pressure–electrochemistry coupling in solid-state lithium metal batteries. *Nat. Rev. Mater.* **9**, 305–320 (2024).
3. Xu, Y. *et al.* Grid-scale corrosion-free Zn/Br flow batteries enabled by a multi-electron transfer reaction. *Nat. Energy* **10**, 1470–1481 (2025).
4. Mao, J. *et al.* Reunderstanding Aqueous Zn Electrochemistry from Interfacial Specific Adsorption of Solvation Structures. *Energy Environ. Sci.* **11**, 772–799 (2018).
5. Chen, W. *et al.* A manganese–hydrogen battery with potential for grid-scale energy storage. *Nat. Energy* **3**, 428–435 (2018).
6. Wei, Z. *et al.* From spent Zn–MnO_2 primary batteries to rechargeable Zn–MnO_2 batteries: A novel directly recycling route with high battery performance. *J. Environ. Manage.* **298**, 113473 (2021).
7. Yang, H. *et al.* Protocol in evaluating capacity of Zn–Mn aqueous batteries: A Clue of pH. *Adv. Mater.* **35**, 2300053 (2023).
8. Ren, Y. *et al.* Aqueous MnO_2/Mn^{2+} electrochemistry in batteries: Progress, challenges, and perspectives. *Energy Environ. Sci.* **17**, 425–441 (2024).
9. Ye, X. *et al.* Unraveling the deposition/dissolution chemistry of MnO_2 for high-energy aqueous batteries. *Energy Environ. Sci.* **16**, 1016–1023 (2023).
10. Deng, Y. *et al.* Nanomicellar electrolyte to control release ions and reconstruct hydrogen bonding network for ultrastable high-energy-density Zn–Mn battery. *J. Am. Chem. Soc.* **145**, 20109–20120 (2023).
11. Wang, B. *et al.* High-performance MnO_2-based cathodes for aqueous zinc-ion batteries: Challenges, strategies, and perspectives. *eScience Energy* **1**, 100008 (2025).
12. Guo, X. *et al.* Zn/MnO_2 battery chemistry with dissolution-deposition mechanism. *Mater. Today Energy* **16**, 100396 (2020).
13. Chen, H. *et al.* Achieving highly reversible Mn^{2+}/MnO_2 conversion reaction in electrolytic Zn-MnO_2 batteries via electrochemical-chemical process regulation. *Angew. Chem. Int. Ed.* **64**, e202423999 (2025).
14. Xue, X. *et al.* Interface-controlled redox chemistry in aqueous Mn^{2+}/MnO_2 batteries. *Adv. Mater.* **37**, 2419505 (2025).
15. Li, Y. *et al.* In situ formation of liquid crystal interphase in electrolytes with soft templating effects for aqueous dual-electrode-free batteries. *Nat. Energy* **9**, 1350–1359 (2024).
16. Chuai, M. *et al.* Design of a P–O–M (M = Mn, Zn) d-pπ backbonding electrolyte additive for 40 Ah electrolytic Zn–MnO_2 batteries. *J. Am. Chem. Soc.* **147**, 31591–31602 (2025).
17. Xiao, X. *et al.* Ultrahigh-loading manganese-based electrodes for aqueous batteries via polymorph

tuning. *Adv. Mater.* **35**, 2211555 (2023).
18. Chao, D. *et al.* Atomic engineering catalyzed MnO_2 electrolysis kinetics for a hybrid aqueous battery with high power and energy density. *Adv. Mater.* **32**, 2001894 (2020).
19. Kong, S. *et al.* Acid-stable manganese oxides for proton exchange membrane water electrolysis. *Nat. Catal.* **7**, 252–261 (2024).
20. Song, Y. *et al.* Stabilizing lattice oxygen to enable durable MnO_2 electrocatalyst for simultaneous acidic hydrogen production and biomass valorization. *Angew. Chem. Int. Ed.* **64**, e202502847 (2025).
21. Grimaud, A. *et al.* Activating lattice oxygen redox reactions in metal oxides to catalyse oxygen evolution. *Nat. Chem.* **9**, 457–465 (2017).
22. Zhang, N. *et al.* Lattice oxygen activation enabled by high-valence metal sites for enhanced water oxidation. *Nat. Commun.* **11**, 4066 (2020).
23. Chen, K. *et al*. Morphology engineering of high performance binary oxide electrodes. *Phys. Chem. Chem. Phys.* **17**, 732–750 (2014).
24. Hill, L. I. & Verbaere, A. On the structural defects in synthetic γ-MnO_2s. *J. Solid State Chem.* **177**, 4706–4723 (2004).
25. Kim, C.-H. *et al.* The structure and ordering of ε-MnO_2. *J. Solid State Chem.* **179**, 753–774 (2006).
26. Chen, H. *et al.* Reunderstanding the reaction mechanism of aqueous Zn–Mn batteries with sulfate electrolytes: Role of the zinc sulfate hydroxide. *Adv. Mater.* **34**, 2109092 (2022).
27.Fetisov, V. *et al.* Electrochemical dissolution of Mn_3O_3 in acid solutions. *J. Solid State Electrochem.* **11**, 1205–1210 (2007).
28. Gao, T. *et al.* A comparison study on Raman scattering properties of α- and β-MnO_2. *Anal. Chim. Acta* **648**, 235–239 (2009).
29. Pahari, S. K. & Chen, Y.-T. *In situ* spectroelectrochemical detection of oxygen evolution reaction intermediates with a carboxylated graphene–MnO_2 electrocatalyst. *ACS Appl. Mater. Interfaces* **14**, 5177–5182 (2022).
30. Xie, K. *et al.* Decoding "dead Mn" in MnO_2 deposition/dissolution chemistry for energetic aqueous batteries: A perspective. *Energy Mater. Devices* **3**, 9370071 (2025).
31. Wang, J. *et al.* Unlocking superior proton-storage contribution and structure stability by synergistic dual-ion modulation in δ-MnO_2 cathodes for aqueous zinc-ion batteries. *Mater. Today Energy* **53**, 102027 (2025).
32. Chao, D. *et al.* An electrolytic Zn–MnO_2 battery for high-voltage and scalable energy storage. *Angew. Chem. Int. Ed.* **58**, 7823–7828 (2019).
33. Wu, D. *et al.* Simultaneous elucidation of solid and solution manganese environments via multiphase *operando* extended X-ray absorption fine structure spectroscopy in aqueous Zn/MnO_2 batteries. *J. Am. Chem. Soc.* **144**, 23405–23420 (2022).
34. Wang, Z. Distribution of relaxation times for impedance analysis in batteries and fuel cells. *Nat.*

Rev. Clean Technol. **1**, 453–453 (2025).

35. Soni, R. *et al.* Lithium-sulfur battery diagnostics through distribution of relaxation times analysis. *Energy Storage Mater.* **51**, 97–107 (2022).
36. Chen, J. *et al.* Charging processes in lithium-oxygen batteries unraveled through the lens of the distribution of relaxation times. *Chem* **9**, 2267–2281 (2023).
37. Sun, C. *et al.* D. Tunnel-dependent supercapacitance of MnO_2 : effects of crystal structure. *J. Appl. Crystallogr.* **46**, 1128–1135 (2013).
38. Liu, Y. *et al.* High-voltage manganese oxide cathode with two-electron transfer enabled by a phosphate proton reservoir for aqueous zinc batteries. *ACS Energy Lett.* **7**, 1814–1819 (2022).
39. Wang, Q. *et al.* Rescue of dead MnO_2 for stable electrolytic Zn–Mn redox-flow battery: a metric of mediated and catalytic kinetics. *Natl. Sci. Rev.* **11**, nwae230 (2024).
40. Zeng, X. *et al.* Toward a reversible Mn^{4+}/Mn^{2+} redox reaction and dendrite-free Zn anode in near-neutral aqueous Zn/MnO_2 batteries via salt anion chemistry. *Adv. Energy Mater.* **10**, 1904163 (2020).
41. Qin, Y. *et al.* Manganese as electron reservoir stabilized $RuMnO_x$@RuO_x with enhanced activity and robust durability for acidic water oxidation. *ACS Catal.* **14**, 12970–12981 (2024).
42. Su, H. *et al.* Tensile straining of iridium sites in manganese oxides for proton-exchange membrane water electrolysers. *Nat. Commun.* **15**, 95 (2024).
43. Kohler, T. *et al.* Hydrogen bonding and Jahn–Teller distortion in groutite, *α*-MnOOH, and manganite, *γ*-MnOOH, and their relations to the manganese dioxides ramsdellite and pyrolusite. *J. Solid State Chem.* **133**, 486–500 (1997).
44. Li, Y. *et al.* A progressive nucleation mechanism enables stable zinc stripping–plating behavior. *Energy Environ. Sci.* **14**, 5563–5571 (2021).
45. Li, J. *et al.* Ferromagnetic ordering correlated strong metal–oxygen hybridization for superior oxygen reduction reaction activity. *Proc. Natl. Acad. Sci.,* **120**, e2307901120 (2023).
46. Kanazawa, K. *et al.* Frequency of a quartz microbalance in contact with liquid. *Anal. Chem.* **57**, 1770–1771 (1985).
47. Srivastava, A. K. & Sakthivel, P. Quartz-crystal microbalance study for characterizing atomic oxygen in plasma ash tools. *J. Vac. Sci. Technol. A* **19**, 97–100 (2001).
48. Kresse, G. & Furthmüller, J. Efficient iterative schemes for ab initio total-energy calculations using a plane-wave basis set. *Phys. Rev. B* **54**, 11169–11186 (1996).
49. Hammer, B. *et al.* Improved adsorption energetics within density-functional theory using revised Perdew-Burke-Ernzerhof functionals. *Phys. Rev. B* **59**, 7413–7421 (1999).

Supplementary Files

This is a list of supplementary files associated with this preprint. Click to download.

- SupplementaryInformation.pdf